Journal of Volcanology and Geothermal Research 435 (2023) 107769

Contents lists available at ScienceDirect

Journal of Volcanology and Geothermal Research

journal homepage: www.journals.elsevier.com/journal-of-volcanology-and-geothermal-research

Assessing the potential to detect vertical magma migration using seismicity through the analysis of the seismic network design

K.E. James [a,*], T. Espinosa-Ortega [a], C.T. Tan [c], B. Taisne [a,b]

[a] Earth Observatory of Singapore, Nanyang Technological University, Singapore
[b] Asian School of the Environment, Nanyang Technological University, Singapore
[c] Science Centre Board, Singapore

ARTICLE INFO

Keywords:
SARA
Magma migration
Volcanic Hazard
Seismic Network monitoring

ABSTRACT

Seismic swarms triggered by magma migration at volcanoes often imply an impending eruption. Using Seismic Amplitude Ratio Analysis (SARA) we have a tool to detect these migrations without having to do in-depth analysis of seismograms. This study examines the detection capability of SARA and introduces a new method to quantify it for different seismic network designs for different magma migrations. This is computed using the location of the seismic stations as well as a detection threshold defined using real swarm data. As an example, we applied the analysis to the Piton de la Fournaise seismic network and computed the volume under the volcano where the seismic network is capable to detect vertical migrations. Moreover, we evaluated the impact removing or adding seismic stations has on the detection capability of the network. This method provides a quick and straightforward way for volcano observatories to identify any detection gaps in a network, as well as providing a way to identify the type of migration event a network is most likely to detect.

1. Introduction

Volcanic eruptions are frequently preceded by magma migration towards the surface, inducing stress perturbations in the surrounding rock (Rubin and Gillard, 1998) that create brittle fractures and trigger seismic swarms. Thus, seismic migrations are often related to magma dynamics (Benoit and McNutt, 1996; Tanaka et al., 2002; Passarelli et al., 2018; Métaxian et al., 2020) but are not exclusive (Zobin and Sudo, 2017). However, during a real-time seismic crisis, the intensity of the seismic activity leads to an overlap of the seismic events which prevents the identification of hypocentres by phase arrival time differences for volcanic tremor earthquakes associated to magma movement (Koyanagi et al., 1987; Lahr et al., 1994). Therefore, it is crucial for the observatories to have alternative methods to analyse the continuous seismic waveform that allow the fast identification of magma migration.

The amplitude decay of the seismic waves allows for the location of seismic sources without the need to compute the travel time delays (Yamasato, 1997; Jolly et al., 2002; Battaglia and Aki, 2003). Studies have made use of this effect to locate high frequency seismic events related to magma movements (Battaglia and Aki, 2003, Battaglia et al., 2005a, Battaglia et al., 2005b; Kumagai et al., 2011, 2013; Ogiso and Yomogida, 2012; Kurokawa et al., 2016, Eibl et al., 2017). The amplitude source location method (ASL) used in these studies makes direct use of the seismic amplitudes and require corrections due the amplification factors of individual stations (Kumagai et al., 2013; Walsh et al., 2017).

The Seismic Amplitude Ratio Analysis (SARA) method developed by Taisne et al. (2011) provides a method to image the dynamics of seismic propagation as it happens and allows us to infer the position of eruptive fissures in real-time using the amplitude ratio between two stations to cancel out the source amplitude and reduce the amplification factors effects. Previous SARA studies demonstrated successful applications of the method in detecting the migration of seismic sources related to magma movement (Caudron et al., 2015; Ichihara and Matsumoto, 2017; Caudron et al., 2018; Tan et al., 2019) however, past studies do not provide any spatial constraints for successful SARA, limiting widespread applications. Furthermore, consideration of station locations, when designing a seismic network, for maximising migration detection capability, could be assessed. Therefore, this paper provides a strong basis for quantifying where the limits are for an optimal use of SARA, and for assessing how adding or removing a station from a network impacts its migration detection capability. Our study expands on the current SARA method to create a SARA detection capability tool which assesses the potential of a network to detect seismic migration. Our

* Corresponding author.
E-mail address: kjames3985@gmail.com (K.E. James).

https://doi.org/10.1016/j.jvolgeores.2023.107769
Received 29 September 2022; Received in revised form 3 February 2023; Accepted 7 February 2023
Available online 10 February 2023

general model accounts for the variability, length and direction of the possible seismic migrations and the number of seismic stations needed to effectively detect the trend in the seismic amplitude ratio. The output of our tool defines a volume (referred to as 'detection capability volume') which represents all locations with detection capability, defined as a region where we can detect a given, or longer, migration for a given network geometry. The results will inform volcano observatories whether it is likely to detect a specified, or longer, migration of seismicity beginning from anywhere within the detection capability volume.

As an example, we apply our analysis to a subgroup of 10 stations of Piton de la Fournaise's seismic network. We provide the detection capability volume for vertical magma migrations of different lengths considering variability in event location along the path. The methodology could be applied to more complex migrations that are not covered in the present study. Our research aims to provide a tool for volcano observatories to test the SARA detection capability of their seismic networks using only synthetic data and different migration scenarios.

2. Methodology

2.1. Seismic amplitude ratio for a pair of stations

The SARA approach (as described in Taisne et al., 2011) uses the differences in seismic amplitudes recorded at different stations (Station 1 and Station 2) due to seismic attenuation (Battaglia and Aki, 2003) to detect seismic migrations. Eq. (1) defines the amplitude ratio for a specified source and station locations.

$$\frac{A_1}{A_2} = \frac{r_2^{\,n}}{r_1^{\,n}} e^{-Br_1 + Br_2} \tag{1}$$

where A_i (with $i = 1,2$) is the mean amplitude of the seismic event recorded at the station S_i (Fig. 1), r_i is the distance between the source and the station and the exponent n is equal to 1 for body waves and 0.5 for surface waves. $B = (\pi f)/(Q\beta)$, where f is the mean frequency, Q is the quality factor for attenuation, and β is the shear-wave velocity (Aki and Richards, 1980). The Q factor for attenuation is frequency dependent (Aki and Chouet, 1975) and can be estimated by calculating the amplitude decay over a given distance (Koyanagi et al., 1995).

The amplitude A_i, that appears in Eq. (1) can be obtained from the (3 or 1) velocity component seismogram by calculating the envelop of a band-passed filtered signal and integrating over a time window larger than the differential travel time (Battaglia and Aki, 2003; Taisne et al., 2011). If the instrument and site response are removed from the amplitude, the SARA method can be used to locate events (Taisne et al., 2011; Caudron et al., 2015). Otherwise, it can be used to alert in changes of the seismic location (Tan et al., 2019). In our analysis we calculate the theoretical seismic amplitudes directly from Eq. (1). We chose the parameters values estimated from PdF's January 2010 eruption by Taisne et al. (2011), that used band-passed data between 5 and 15 Hz ($n = 1$, Q = 170, f = 10 Hz, β = 1700 m/s).

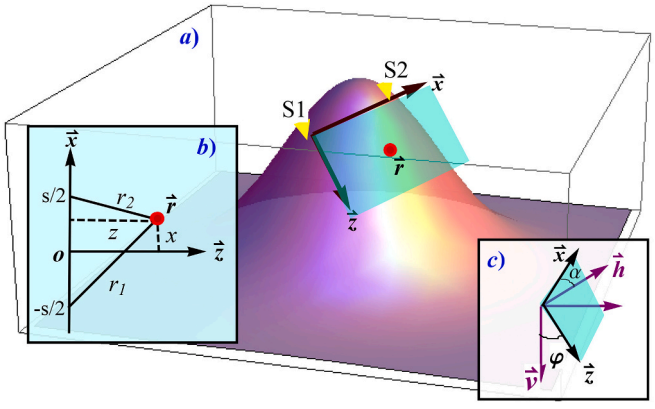

Fig. 1. a) Plane defined by the location of the seismic stations S_1, S_2 (on the flank of a theoretical volcano, highlighted by the surface) and the source of the seismic event (red dot) located at $\mathbf{r} = (x,z,\varphi)$. b) Reference frame: The $\hat{\mathbf{x}}$ axis is along the line that joins the seismic stations, the $\hat{\mathbf{z}}$ axis is perpendicular to the $\hat{\mathbf{x}}$ axis and within the same plane as the vector **r**, φ is the angle between **z** axis and the vertical direction. c) If the altitude of the stations is different, the $\hat{\mathbf{x}}$ axis will make an angle α with respect to the horizontal axis $\hat{\mathbf{h}}$. In the case $\alpha = \varphi = 0$, the $\hat{\mathbf{x}}$ axis is along the horizontal axis and $\hat{\mathbf{z}}$ is along the depth direction. (For interpretation of the references to colour in this figure legend, the reader is referred to the web version of this article.)

By tracking the amplitude ratios (Eq. (1)) through time, and between different pairs of stations, it is possible to infer seismic migration. We assume constant crustal properties (i.e. isotropic medium), as well as a high frequency isotropic radiative pattern for the s-wave seismic energy, since Eq. (1) is valid only in this regime (Morioka et al., 2017). Therefore f, Q, β and thus B are considered constant.

As shown in Fig. 1 a the location of the pair of stations and the seismic event source defines a plane that can be used as a reference frame (Fig. 1 b) to explore the variation of the amplitude ratio. For a pair of stations separated by a distance s, and a seismic source with coordinates $\mathbf{r} = (x,z,\phi)$, we have:

$$r_1 = \sqrt{z^2 + (x + s/2)^2} \tag{2}$$

$$r_2 = \sqrt{z^2 + (x - s/2)^2} \tag{3}$$

Notice that since the ratios only depend on x and z, the problem has a cylindrical symmetry and the ratios are independent of the azimuth angle ϕ, around the axis x that joins both stations. Notice that the direction of this axis depends on the height difference of the stations. In general, the axis x will have an angle α with respect to the horizontal line.

Substituting Eqs. (2,3) into Eq. (1), we can calculate the amplitude ratio for a "body" ($n = 1$) S wave seismic source at different positions (see Fig. 2 a).

In a migration episode, the seismic source location continuously shifts along a given direction. The amplitude ratio change depends greatly on the path of the migration. Theoretically, if the magma path is along the contour lines of the amplitude ratio, the value of A_1/A_2 will remain constant as is the case of the magma paths P_0 and P_1, as shown in Fig. 2 b. Moreover, the amplitude ratio will also remain constant if the magma migration path moves along the azimuth angle ϕ, while keeping (x,z) constant. In contrast, if the magma migration follows a direction that crosses the contour lines of Eq. (1), there will be an amplitude ratio trend as is the case for P_2, P_3 and P_4.

Vertical magma migrations are of particular interest since they can mark an impending eruption. If the magma source is located exactly below the line that joins the stations ($\phi = 0$) and that line is parallel to the horizon (i.e. the stations have the same altitude or the difference is neglectable so $\alpha \sim 0$ in Fig. 1 c), the **z** axis direction will be equal to the depth and the path of the vertical magma migration will be similar to P_3 (the path P_0 is a unique case when the migration is equidistance to the stations). Nevertheless, often the altitudes of the pair of stations are quite different and thus the vertical migration of magma won't be parallel to the **z** axis but along an oblique line similar to the paths P_2 or P_4 (see Figs. 2 a & b). The maximum change is along the gradient of A_1/A_2 as shown in Fig. 2 c, since this is the direction and rate of higher increase of Eq. (1). Most volcanic seismic networks are composed of several stations; thus, the amplitude ratio will vary from station pair to another according to each pair's symmetry. The location of the pair of stations might favour the detection in certain directions like side vents (along the axis that joins the stations) and could potentially obscure other migration paths.

Another consideration is that in real magma migration events the

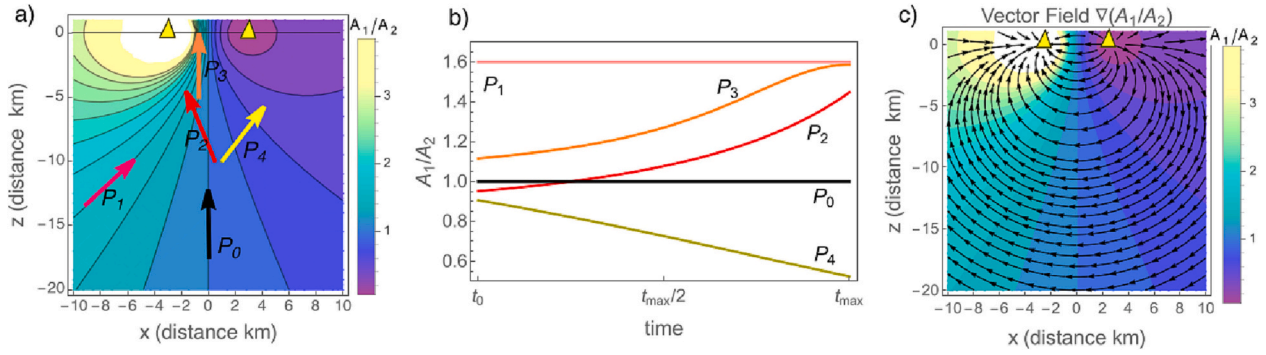

Fig. 2. a) Contour plot of the seismic amplitude ratio for an arbitrary pair of stations (yellow triangles) separated by 5 km, the colours indicate the value of Eq. (1) for different seismic source positions $\mathbf{r} = (x, z)$. The arrows indicate 5 possible magma paths P_i. b) Amplitude ratio as a function of time for the magma paths P_i. c) Vector field equal to $\nabla\left(\frac{A_1}{A_2}\right) = \partial_x\left(\frac{A_1}{A_2}\right)\hat{x} + \partial_z\left(\frac{A_1}{A_2}\right)\hat{z}$. Parameters used: $n = 1$, Q = 170, f = 10 Hz, β = 1700 m/s. (For interpretation of the references to colour in this figure legend, the reader is referred to the web version of this article.)

amplitude ratio would have some variability due to a non-perfect migration route, other unrelated seismic events and/or spread seismic sources along the migration (Rubin, 1993), see Fig. 3. This variability in the ratio and symmetry considerations limit the station pairs' ability to detect migrations with small changes in amplitude ratios, and hence less obvious amplitude ratio trends are easily obscured, making it difficult to distinguish between a ratio change due to migration and that due to natural variability.

In summary, there is a realistic boundary within which SARA could be effectively employed, and therefore, it is useful to have a detection capability tool – SARA Detection Capability Tool - that assesses the ability of the station network to detect a given migration confidently.

2.2. SARA Detection Capability of a seismic network

In this section we define the SARA detection capability of a seismic network. Instead of using the amplitude ratios for a station pair directly, we use the absolute log of the amplitude ratios (LAR, see Eq. 4), since by taking the absolute log value, the LAR is the same for each pair of stations disregarding the station pair order:

$$\mathrm{LAR}(\mathbf{r}) = \left|log_{10}\left(\frac{\mathrm{A}_1(\mathbf{r})}{\mathrm{A}_2(\mathbf{r})}\right)\right| = \left|log_{10}\left(\frac{\mathrm{A}_2(\mathbf{r})}{\mathrm{A}_1(\mathbf{r})}\right)\right|, \tag{4}$$

We also define the LAR difference (ΔLAR) as the change of the LAR when the magma seismic source is at two different positions separated by the distance δ (Eq. 5).

$$\Delta\mathrm{LAR}_\delta(\mathbf{r}) = |\mathrm{LAR}(\mathbf{r}) - \mathrm{LAR}(\mathbf{r} - \delta)| \tag{5}$$

As mentioned before, during magma migration the seismic amplitude ratio (and thus the LAR) will have some variability. For instance, real vertical magma migrating along the path P_3 in Fig. 2 will have a LAR similar to Fig. 3. If the variability for a 1 km migration path is smaller than the corresponding ΔLAR, we will be able to detect the 1 km migration (Fig. 3 a). Otherwise, if the variability for the 1 km path is larger or comparable to the $\Delta\mathrm{LAR}_{1\mathrm{km}}$ as in the 1 km section in Fig. 3 b, then we will not be able to detect the migration, since we won't be able to attribute the change in LAR to a migration.

Therefore, it is necessary to set a minimum detectability threshold for positive detection. Any ΔLAR larger than the detectability threshold is deemed as positive detection as we regard the difference as too large

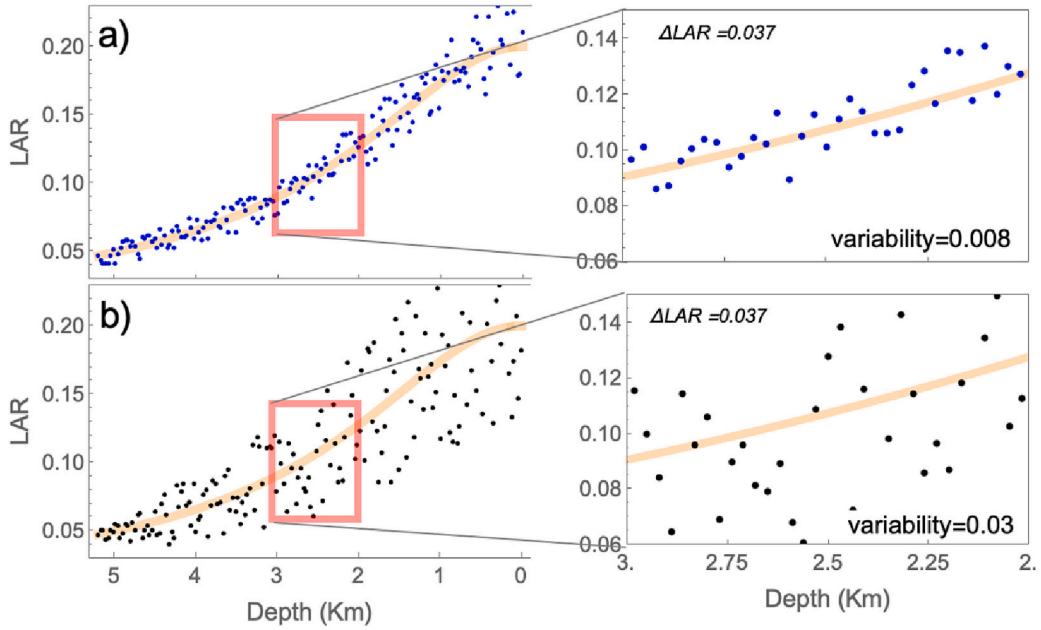

Fig. 3. LAR for an arbitrary pair of stations separated by 5 km showing a vertical magma migration (P_3 in Fig. 2) with small a) and large b) variability. For the magma migration in a) between −3 to -2 km the variability = 0.008, while for the magma migration in b) the variability = 0.03.

to be attributed to natural variability.

As an example, for an arbitrary pair of stations separated by 5 km we calculate the LAR for a seismic source located below the line that joins the stations (Fig. 4). We also calculate the ΔLAR_{1km} for vertical migrations of 1 km starting at different locations (x,z). In other words, at every point in Fig. 4, the ΔLAR_{1km} is the absolute difference in LAR between that point and the point 1 km directly below.

The ΔLAR is greater at shallower depths as the amplitude ratios become increasingly larger with decreasing depth (Fig. 4). In the area enclosed by the curve $\Delta LAR_{1km} = 0.01$, we will have positive detection for 1 km vertical migrations for magma paths with variability (or standard deviation) below the 0.01 threshold. Positive detection for a 1 km migration and a threshold of 0.05 is only possible for depths (starting from the station position) shallower than 5 km and locations a few km around the stations (see the isoline $\Delta LAR_{1km} = 0.05$ in Fig. 4). Thus, a larger variability threshold limits positive detection to shallower depths, and for this example specifically, vertical magma migration paths of 1 km with large variability can only be located in shallower depths. See Appendix for details about how to select an appropriate threshold.

In this case we only consider one pair of stations, however, most seismic networks are composed of several stations. A seismic network of N stations generates N(N-1)/2 different station pairs. Thus, we need to calculate the LAR and ΔLAR for the N(N-1)/2 pairs of stations and for all points of the three-dimensional space where the seismic source could originate from.

2.2.1. Detection capability volume

We can determine the number of station pairs which have positive detection and are able to detect (for instance) a 1 km vertical migration below a certain variability threshold. If enough stations pairs have positive detection, we then deem that the network can detect the migration (positive final detection).

We define the number of 'sufficient' station pairs needed for detection to be the minimum number of stations pairs needed for independence. For a seismic network of N stations, if we have positive detection only for N-1 station pairs then the detection might be due to a single station (since one station generates N-1 pairs). Thus, we require that at least N stations pairs have positive detection ensuring that the output detection is not biased towards a single station. For example, using a ten-station network means a minimum of ten station pairs are necessary for positive final detection.

In summary, for a network of N stations, we have a positive detection at a given point if at least N stations pairs have a ΔLAR ≥ threshold. We then define a detection capability volume (DCV), that encompasses all the starting locations from where it is possible to detect a 1 km (for δ=1 km) or longer migration, beginning from anywhere within the volume.

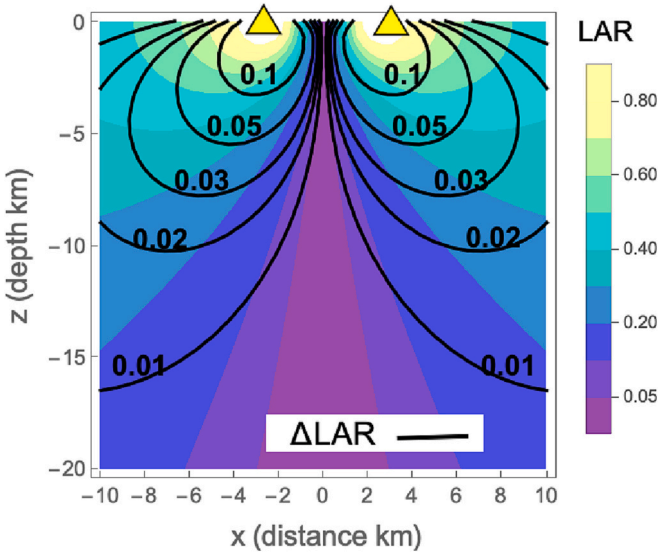

Fig. 4. LAR for 2 arbitrary stations (yellow triangles), separated by 5 km and located at sea level (i.e., Depth = 0 km). The colours indicate the value of LAR for a seismic source at different depths and horizontal distances (x, z). The thick-black lines indicate value of the isolines of the ΔLAR for horizontal migrations of δ =1 km (in the z direction, see Eq. 5), i.e., $\Delta LAR_{1km} = 0.1$, $\Delta LAR_{1km} = 0.05$, etc. (For interpretation of the references to colour in this figure legend, the reader is referred to the web version of this article.)

2.2.2. Factors that influence the DCV

To explore the relation between the detection capability volume, the threshold and the vertical migration length, we use as an example two synthetic 5-station seismic network configurations as shown in Fig. 5. In this example all the stations of the seismic network are located at sea level, and we consider all vertical migrations starting at any point below the sea level. First, we calculate the DCV as a function of the threshold and different vertical migration lengths (Fig. 5 a). We observe how increasing the threshold decreases the DCV, and how increasing the vertical migration length increases the DCV.

We further explore the dependence of the DCV as a function of the station interspacing, thus we perform the same calculations but increase the distance between the seismic stations (as shown in Fig. 5 b). We found that increasing the interspacing increases the DCV. Nevertheless, is important to note that in this example the stations are located at the same altitude whereas the topography of the volcanoes can vary greatly and thus any change in the east-west or north-south direction will also imply a change in altitude.

3. Results

3.1. Application to the seismic network of Piton de la Fournaise

We apply our analysis to a subgroup of the PdF seismic network (OVPF & IPGP, 2008) shown in Fig. 6. This subgroup consists of 10 stations chosen for being closest to the summit; thus, we have a total of 45 different station pairs for which we calculate the LAR and the ΔLAR.

As migrations often occur beneath the summit, we first simulate a vertical migration directly under the summit from a starting depth of 10 km below sea level (bsl). In Fig. 7 we show the computed LAR and ΔLAR_{1km} for each pair of stations in the seismic network, for this specific vertical magma migration. As explained previously ΔLAR_{1km} is equal to the difference between the LAR at any given point, and the LAR 1 km below (Eq. 5 with δ=1 km for the coordinate towards the depth direction).

The choice of the threshold is fundamental to define the positive detection. The threshold is related to the expected variability of the magma paths; for PdF we use real data (Tan et al., 2019) from a short migration episode that was recorded on July 31, 2015 (See Appendix & Fig. S1). We compute the variability of the detrended LAR and found a standard deviation ~0.1. Thus, for our analysis we select a threshold = 0.1.

In Table 1 we show the final positive detection for different starting depths. For instance, a 1 km vertical migration below the PdF summit starting at 10 km bsl the $\Delta LAR_{1km} < 0.1$ for all the 45 station pairs and thus we have no final positive detection. For the vertical migration that starts at 1 km bsl the $\Delta LAR_{1km} > 0.1$ for 3 station pairs only, thus again there is no final positive detection. This changes for migrations starting at sea level where we have 10 station pairs with positive detection and thus, we do have final positive detection.

3.1.1. Vertical migrations

We extend the analysis by computing the network's ability to detect migrations of at least 1 km long starting anywhere below the PdF's surface. In other words, we compute the ΔLAR at every point in a three-dimensional grid and select the points where the $\Delta LAR_{1km} \geq$ threshold

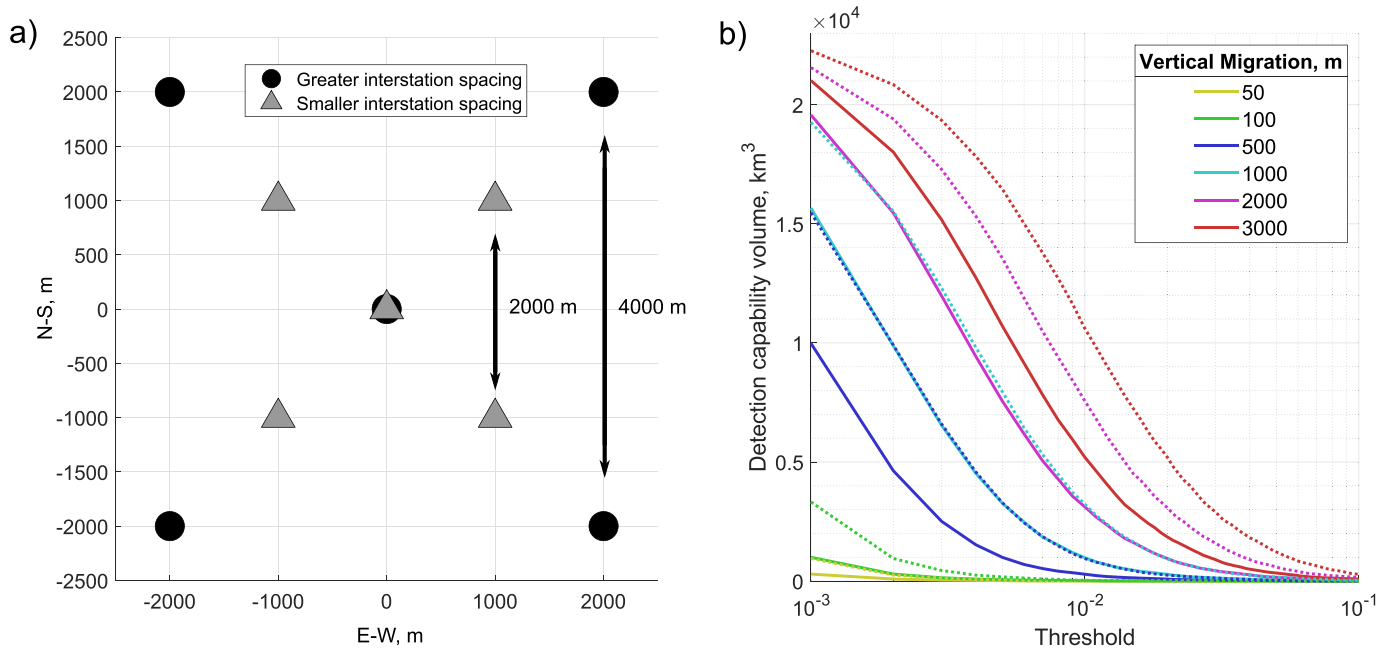

Fig. 5. a) Two synthetic networks. The two networks are identical in shape but have different distances between the stations. b) The relationship between DCV, migration length and threshold for the two synthetic symmetrical five station networks. Data for the network with the better detection capability, and the greater interstation distance, is shown by the circle markers in 5a) and the dotted lines in 5b).

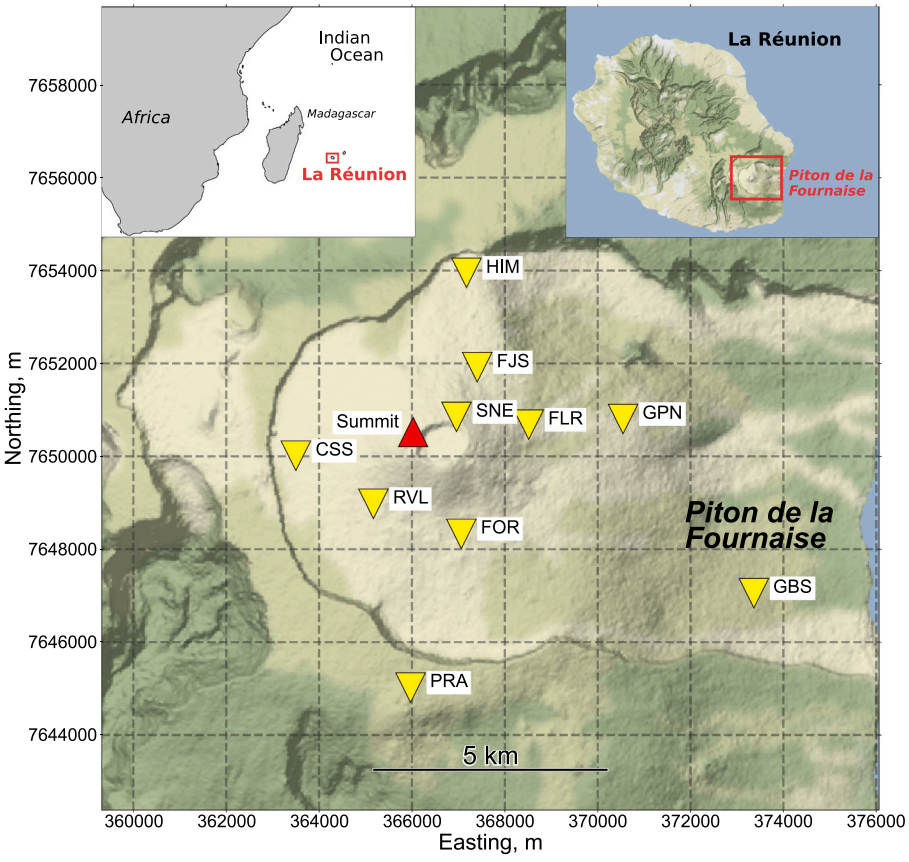

Fig. 6. Location and seismic network (inset) map of Piton de la Fournaise (IPGP). The stations in Standard UTM 40S (easting, northing, elevation): CSS (363,499, 7,650,012, 2193), FJS (367,405, 7,651,918, 2123), FLR (368,515, 7,650,682, 1947), FOR (367,062, 7,648,331, 2049), GBS (373,364 7,647,052, 471), GPN (370,546, 7,650,803, 1413), HIM (367,174, 7,653,950, 1958), PRA(365,969, 7,645,020, 2009), RVL(365,170, 7,648,977, 2110), SNE (366,958, 7,650,849, 2505). Summit (in red) location: (366,026, 7,650,467). (For interpretation of the references to colour in this figure legend, the reader is referred to the web version of this article.)

for at least 10 stations (Fig. 8).

This inherently implies that at all locations within the obtained DCV, any vertical migration equal to or >1 km can be detected. Similar analysis could be performed for other migration paths by changing the Δ magnitude and direction in Eq. 5. The DCV reflects the network's SARA detection capability. In general, the more locations that have positive

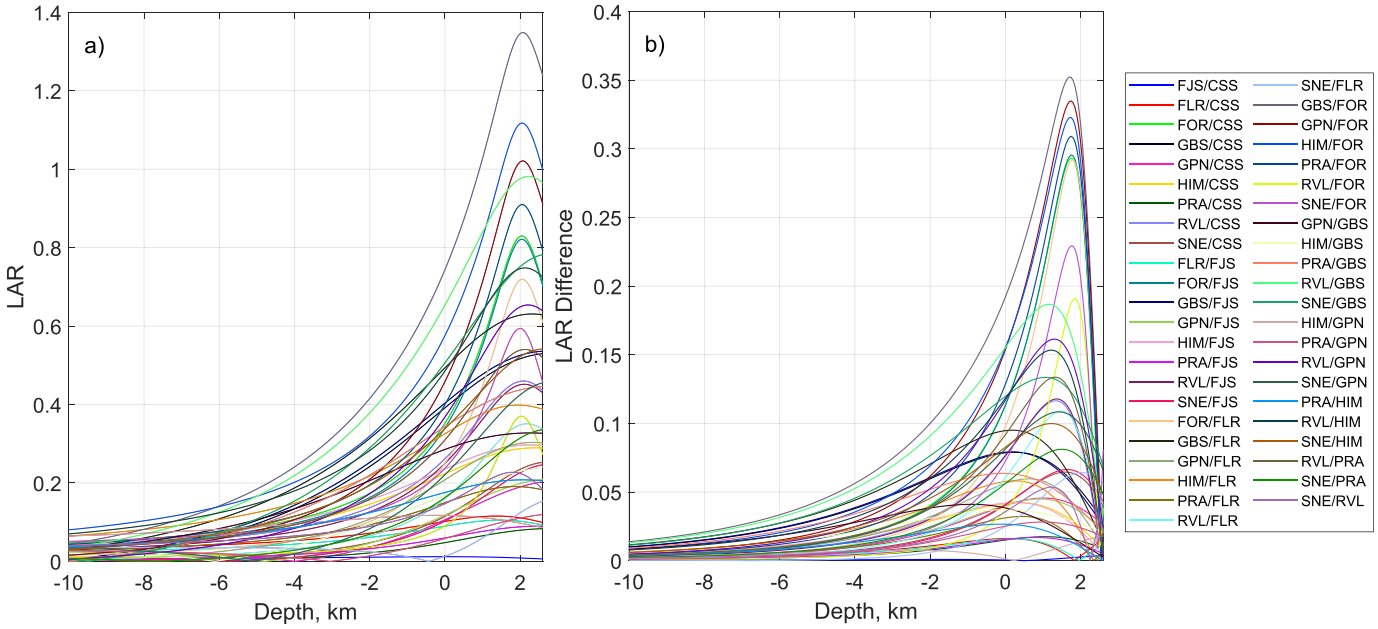

Fig. 7. a) LAR for a vertical magma migration path located directly below the PdF summit (2.3 km above sea level). b) ΔLAR for 1 km vertical migrations located directly below the PdF summit, the coloured lines indicate the station pair as described in the inset.

Table 1
Depth and final detection. Values are for a 1 km magma vertical migration location directly beneath the PdF summit, threshold of 0.1.

Finishing Depth	No. of pairs with positive detection	Final Positive Detection
1 0 km bsl	0	No
1 km bsl	3	No
0 km	10	Yes

final detection, the greater the DCV, the better the detection capability of the whole network. Additionally, where the DCV is situated is important. A large DCV far away from expected migration locations might be less effective in detecting migrations than a small DCV near to expected migration locations, reflecting poorer detection capability.

The DCV for 1 km vertical migrations are shown in Fig. 8. With a detectability threshold of 0.1, the DCV obtained indicates that migrations at least 1 km long in the north-east and south-west can be detected by the network, with the DCV extending approximately 4 km north and south. There is weaker detection capability in the north-west and no detection capability directly beneath or near stations GBS and PRA.

Additionally, vertical detection capability is reasonable with the maximum and minimum depths of the DCV situated at 2.3 km above sea level (summit elevation) and 0.7 km bsl respectively. Vertical detection capability increases the further you horizontally travel from the summit. Detection is weaker directly beneath the summit as there are no seismic stations directly on PdF's summit. Even though the depth of the DCV

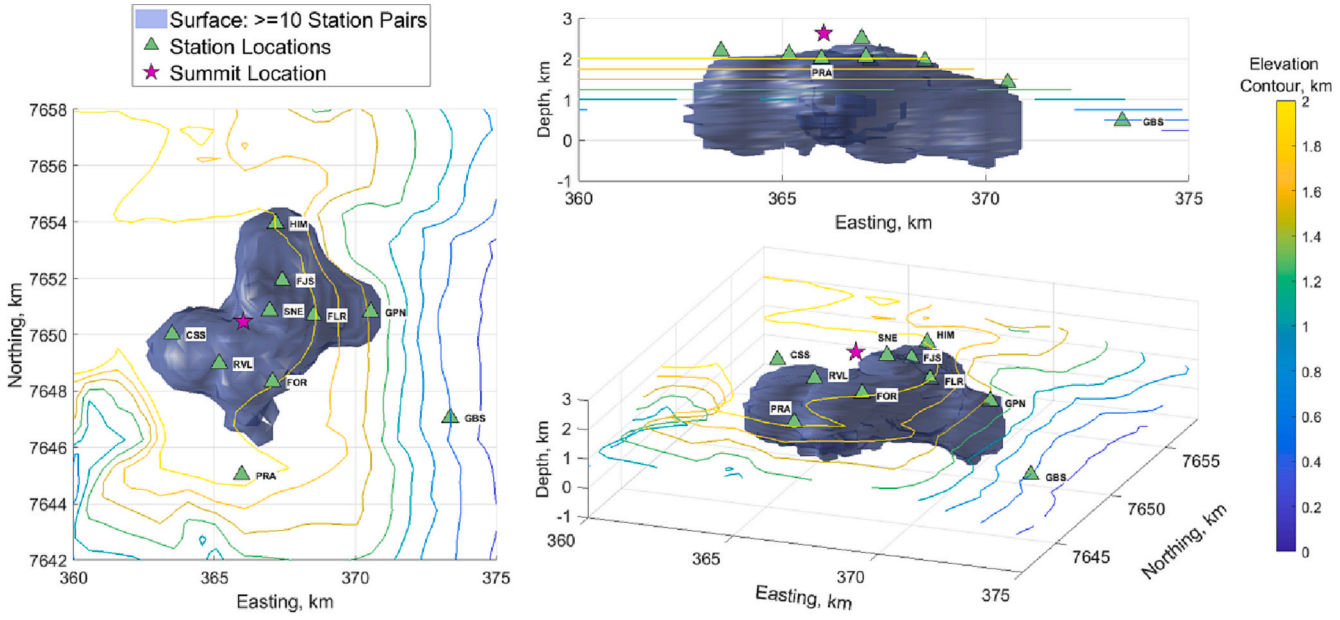

Fig. 8. DCV for the PdF network, for all vertical migrations of 1 km and a threshold = 0.1 for positive detection. The contour lines show the elevation and are at 250 m intervals.

does not extend to depths >0.7 km bsl and the horizontal extent of the DCV is weaker is certain directions, for PdF, this is suitable as seismic swarms are usually shallow, concentrated between 0 and 1 km above sea level in a ring around the summit (Duputel et al., 2019).

3.1.2. Larger vertical migrations for PdF

For larger migrations the DCV is greater in both horizontal and vertical directions as the difference in amplitude ratios become greater and more easily exceed the threshold. We perform the same calculation as described above but for a 2 km and 3 km migration (Fig. 9). Increasing the migration from 1 km to 2 km increases the DCV by a factor of 5 extending the coverage to include station PRA. Additionally, the maximum depth of the DCV increases by ~2 km. The DCV for a 3 km detection is more circular and uniform than the 1 km migration and covers all stations.

3.1.3. Different thresholds for PdF

Using a higher detectability threshold of 0.15 (for 1 km migrations) greatly decreases the DCV (Fig. 10) and instead of having one volume there are now four smaller disconnected volumes that do not cover the summit. If actual migrations produced LAR with variability about this threshold value, then the current network would not be able to detect fluid migrations that occur directly under the summit. However, using a lower threshold of 0.05 improves the coverage as it increases the DCV and increases the uniformity of its shape. Therefore, the choice of threshold strongly controls the shape and size of the DCV. An unsuitable threshold may lead to an inaccurate DCV.

Fig. 11 shows the relationships between the DCV and the detectability threshold for different migration lengths for PdF. A larger threshold value and a smaller migration imposes a more stringent criterion for positive detection (larger ΔLAR are required), resulting in a smaller DCV, and vice versa.

3.2. Assessing the impact of removing or adding stations to a network

To enhance the usefulness of our SARA detection capability tool, we also included the analysis of the impact of station addition or removal to the detection capability of the network as this can influence the detection of seismic migrations (Caudron et al., 2018). Removing stations can tell us: (1) the minimum number of stations needed for the network to remain effective at detecting fluid migrations and (2) which stations are most important for detecting fluid migration within a network. This is useful in the case where more than one station in a network fails, and in identifying the most critical station to maintain. Adding stations helps to inform volcano observatories where to add new stations based off the migration and detection variables they are interested in. We describe the station removal/addition analysis methodology using the network at PdF, with a 1-km vertical migration and a threshold = 0.1.

For the reduced network simulation, we calculate the DCV for a reduced network (with N-1 stations) and compare it to that of the original network (with N stations) (Fig. 12 a). We perform the reduced network simulation N times and remove each station in turn. We use the same code workflow, migration distance and threshold for both the reduced and original network. The only variable which varies is the 'sufficient' number of station pairs. As the reduced network has one less station, the minimum number of station pairs needed for independence is reduced by one; therefore, the number of 'sufficient' station pairs is N-1 for the reduced network and N for the original network.

For the improved network simulation, similarly, we calculate the DCV and centroid of an improved network, N + 1 stations) and compare it to the original network (N stations) (Fig. 12 b). We define where we add the new stations using a two-dimensional grid of points. The new stations are added in turn onto the topography. Like the reduced network simulations, we use the same code workflow for both the improved and original network and the same variables except the number of 'sufficient' station pairs. As the improved network has one

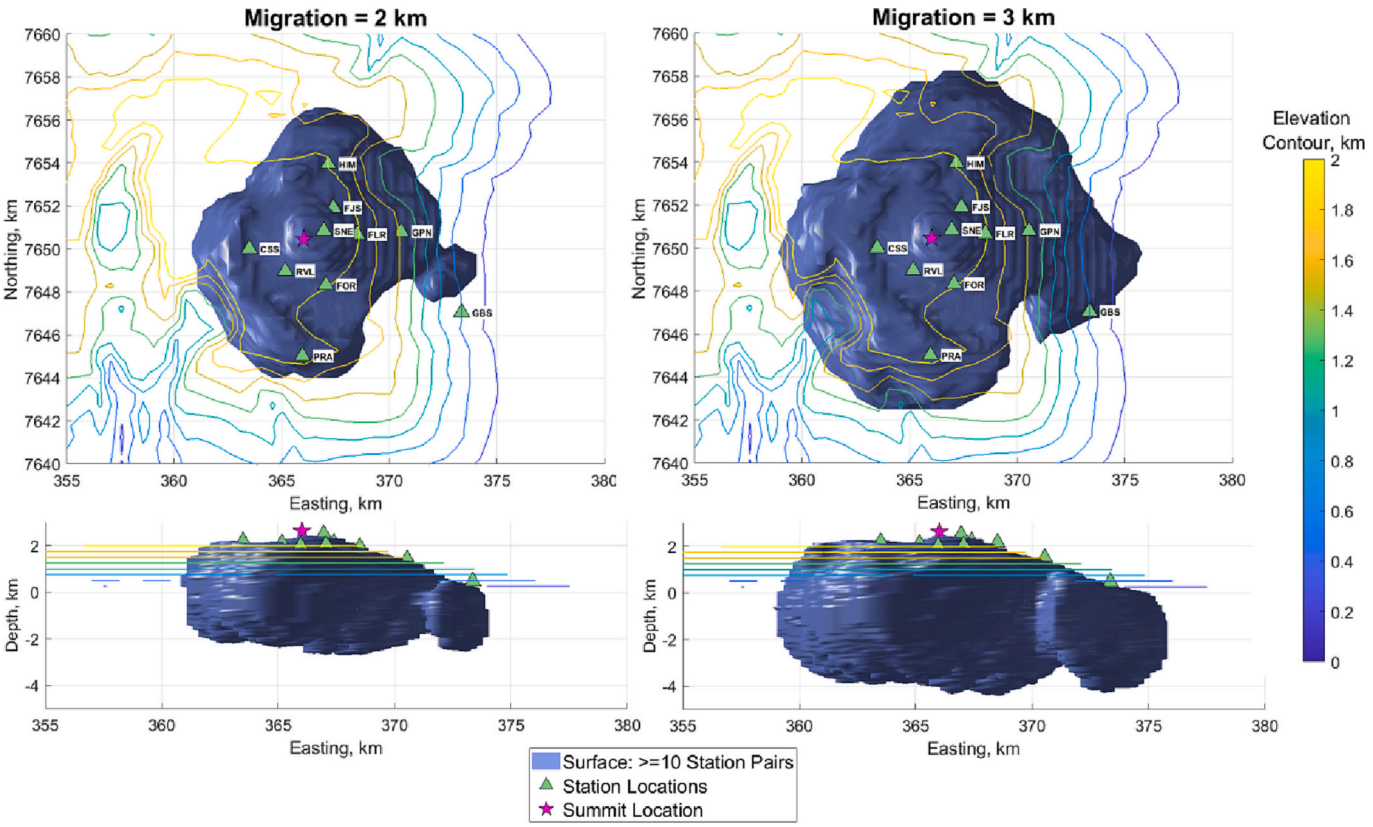

Fig. 9. DCV for any vertical magma migration of 2 km (left) and 3 km (right) for PdF. The contour lines show the elevation and are at 250 m intervals.

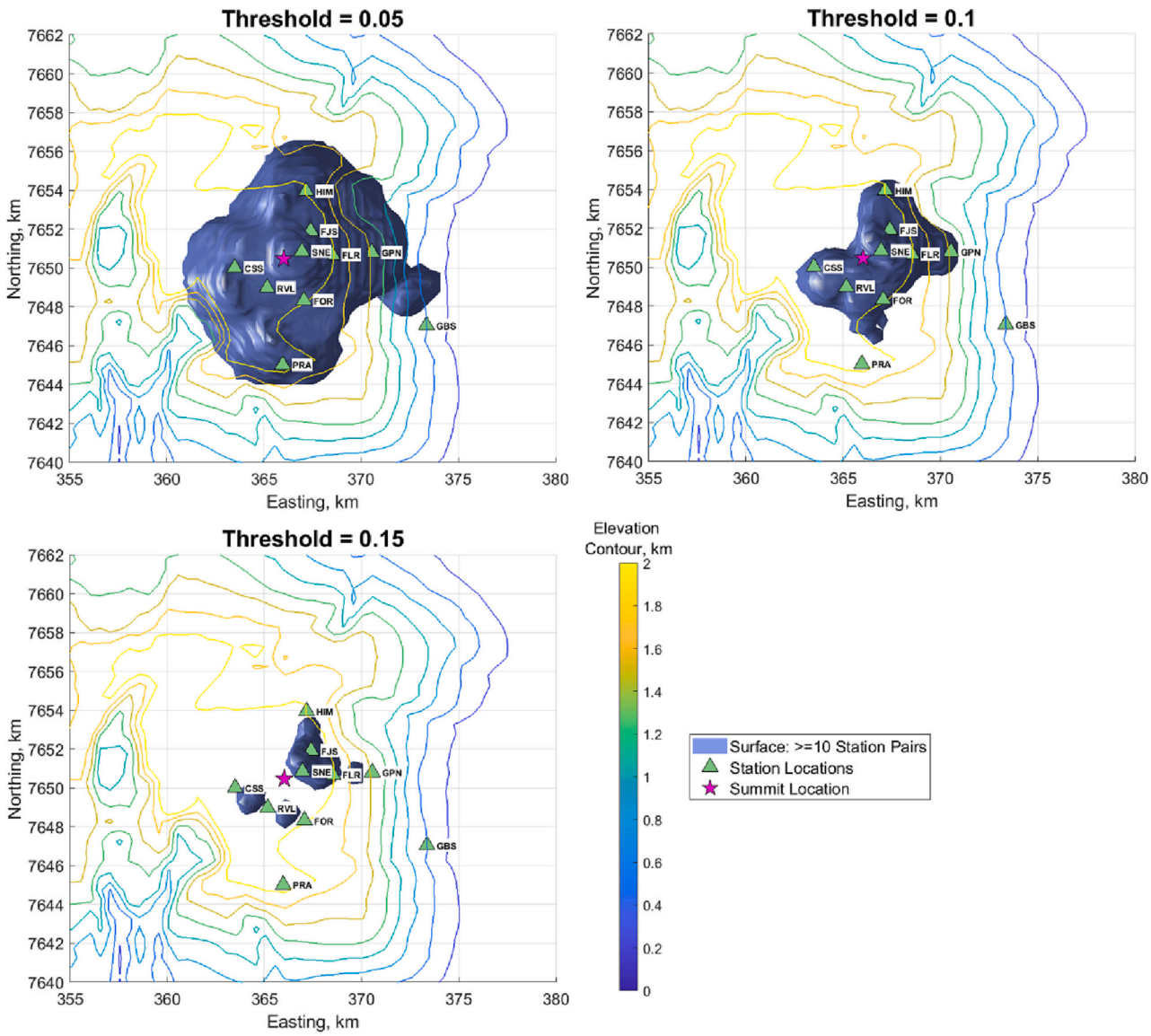

Fig. 10. DCV of the PdF seismic network for different thresholds for a 1 km migration. Increasing the threshold decreases the DCV showing the importance of choosing an accurate threshold. The contour lines show the elevation and are at 250 m intervals.

more station, the number of station pairs necessary for independence is N + 1.

For both the improved and reduced network simulations we quantify the change in detection capability by calculating the change in the DCV. Additionally, we calculate the centroid which is the centre point of the DCV and the centroid shift, which quantifies the change in location of the modified network's centroid compared to the location of the original network's centroid. These allow us to summarise how location of the DCV has changed. In an ideal case, the centroid of the seismic network should be close to the main volcanic conduit.

3.2.1. *Reduced and improved network simulations in PdF*

Removing any station from PdF's seismic network (Fig. 12 a & b) leads to a minimum reduction in the DCV of ~14% demonstrating how important all stations are in this network for maintaining detection capability. Removing stations furthest from the original centroid and summit leads to the greatest reduction in DCV. Removing GBS leads to the greatest reduction in the DCV (37%) even though there is no detection capability at GBS while removing SNE, which is close to the summit, reduces the DCV by 14%. However, removing SNE creates a detection capability 'gap' around the summit. Horizontal centroid shifts when removing any station are small (up to 0.9 km).

For the improved network simulations, we create a grid of stations following the topography of PdF. The grid extends from easting 359.6 km to 374.6 km and northing 7641.8 km to 7657.8 km. Stations were added at 5 km and 4 km intervals respectively (Fig. 12 b). Four locations, (364.6, 7649.8) km, (369.6, 7649.8) km, (364.6, 7641.8) km and (374.6, 7645.8) km have large and similar increases in the DCV (~50–55%) and the added stations in the south lead to larger increases in the DCV. Centroid shifts vary, most shifts are small (< 0.5 km) but adding a station at (364.67645.8) km and (374.6, 7645.8) km shifts the centroid 1.4 km south-west and 1.2 km south-east respectively. Additionally, large variations in the increase in DCV are seen at added stations which are relatively close together. For example, adding a station at (369.6, 7649.8) km increases the DCV by 53% but adding a station 4 km directly north at (369.67653.8) km only increases detection capability by 16%.

As is clear from the calculations shown in Fig. 12, the DCV is highly susceptible to the topography of the volcano as this restricts the location of seismic stations. Shifting one station east or north will imply a change in the altitude that will alter the axis of symmetry. For volcanoes with a highly fluctuating topography the dependence of the DCV on the

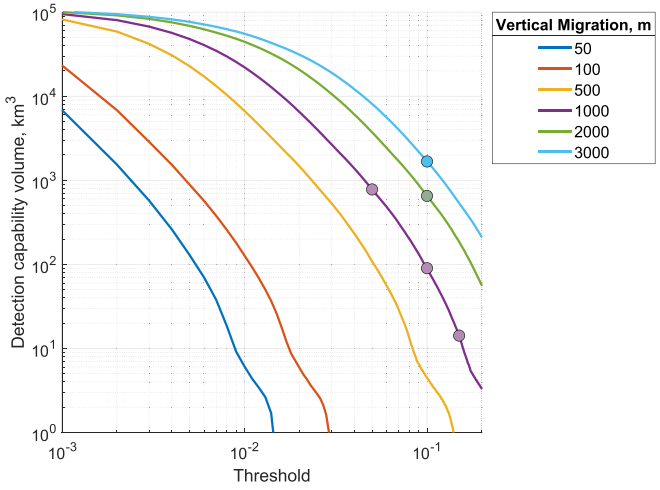

Fig. 11. The relationship between DCV, migration length and threshold for the PdF seismic network. As we increase the value of the threshold, the DCV decreases. The inline colour indicates the different vertical migration lengths (δ = 50 m, δ = 100 m, etc.). The green and blue point corresponds to the DCV calculated using a 2000 m and a 3000 m migration in Fig. 9 respectively. Purple points correspond to DCVs calculated using thresholds of 0.05,0.1 and 0.15 in Fig. 10. (For interpretation of the references to colour in this figure legend, the reader is referred to the web version of this article.)

network configuration will be highly non-linear.

4. Discussion

4.1. Considerations with SARA

We assume that the seismic amplitude decay depends only on the distance between the source and the stations, i.e., we consider as a constant the energy loss due to the anelasticity of the medium (e^B in Eq. (1)) for a S wave isotropic radiation pattern (Morioka et al., 2017). Nevertheless, there can be anisotropy in the seismic energy transport caused by the frequency component (Takemura et al., 2009) or the changes in the shear wave velocity (Bannister et al., 2004; Chávez-García et al., 2007; Godfrey et al., 2017). For seismic waves with high frequency components and seismic stations that are relatively close this effect can be neglected, but the anisotropy can introduce some uncertainties in the ΔLAR for seismic stations far apart. Other sources of uncertainty are the variation of the Quality factor and the amplification factors that can affect the estimated LAR values for isolated stations (Caudron et al., 2018). In addition, in our calculations, we consider only seismic body waves ($n = 1$ in Eq. (1)). However, the exponent of decay n, can change at shallower depths (Hofstetter and Malone, 1986; Jolly et al., 2002) where the surfaces waves can play an important role and thus the values of LAR and ΔLAR can vary, causing small corrections in the DCV.

4.2. Considerations with our method

The detection capability can be influenced by the distance between the seismic source and the station. When the seismic source is far away from the station, the attenuation along the path and perturbations by other unrelated seismic signals will decrease the signal to noise ratio. Thus, the background noise can affect the identification of amplitude ratio changes (Tan et al., 2019) leading to a reduction in detection capability. When performing the simulations of adding or removing a station, we assumed that all the stations have the same ability to detect migration. However, with increasing distance from the seismic migration the signal amplitude decreases and it could become smaller than the background noise. During pre-eruptive magma migrations, if noise was considered the increase in detection capability may be less for stations further away from the seismic migration and adding stations next to the summit (where most of the magma migration occurs) may have had more practical impact on the detection.

An assessment of seismic network coverage should consider not only the absolute value of the DCV but also how this volume relates to the size of the volcano and the coverage of critical areas where lava extrusion has been observed. The definition of the DCV directly depends on the choice of the threshold which is directly related to the variability (or standard deviation) of the amplitude ratio along the migration path (see Appendix). The variability of the amplitude ratio depends on physical constraints controlling the migration (e.g., the stress field, the type of volcano activity, the media) and the location of the migrating fluid relative to the seismic network (that affects the noise at each station). Then, to apply our method, it is essential to carefully choose a threshold value that is comparable to the variability observed in previous real seismic migration episodes. Additionally, when analysing PdF's seismic network we only considered vertical migration, although our formulation is general and other direction migration paths could be also assessed.

4.3. Temporal effects

We do not consider temporal effects related to the duration of the seismic event nor those related to the traveling time from the source to the seismic stations. To calculate the amplitude ratio in Eq. (1) we need to ensure that the seismic signal received at the stations correspond to the same seismic source. This can be achieved by comparing the seismic amplitudes in time-windows longer than the largest differential travel time across the network (Tan et al., 2019) and time-windows with similar variability (Ichihara and Matsumoto, 2017). Moreover, the size of the seismic source for magma migrations is spread along a volume (Rubin, 1993). Consequently, there could be different seismic sources radiating energy simultaneously at different locations making it necessary to use larger time windows (Tan et al., 2019) to compute the amplitude ratio.

The variability of the migrating path can change along the migration path and thus this should be accounted when choosing an adequate threshold and migration length. At PdF vertical migration speeds have been estimated as 0.1 m/s and most fluid migration occurs between 0 and 1 km above sea level near the summit (Duputel et al., 2019), that means it would take ~2.8 h for magma to ascend 1 km. The 0.1 threshold chosen in Section 3.1 is based on the variability of an ~1 h magma path (see Appendix & Fig. S1), if there is no increment of this variability for 2.7 h, a 1 km migration length and 0.1 threshold are good parameters for our detection capability. According to our results this limits the detection to about 2 km below the surface to an area around the summit (Fig. 8) broadly matching the observed data.

5. Conclusion

The detection capability tests performed in this paper defines the spatial extent where SARA can be applied effectively if a threshold can be reliably defined. In addition, expanding on the SARA method to test the effect that adding and removing a station from an existing network has on the detection capability has real life implications. This methodology can inform observatories which stations are most vital in a network and can be used to advise which locations are best for new stations. Hence, if adopted by volcano observatories our methodology will have practical implications.

This paper opens new paths for research involving the detection capability of SARA. Future research could expand on the detection capability method used in this paper to make it more representative of real-life scenarios. This could be done by adding noise and exploring non-vertical migration paths. Additionally, it would be useful to compare the detection capability of this method with more traditional

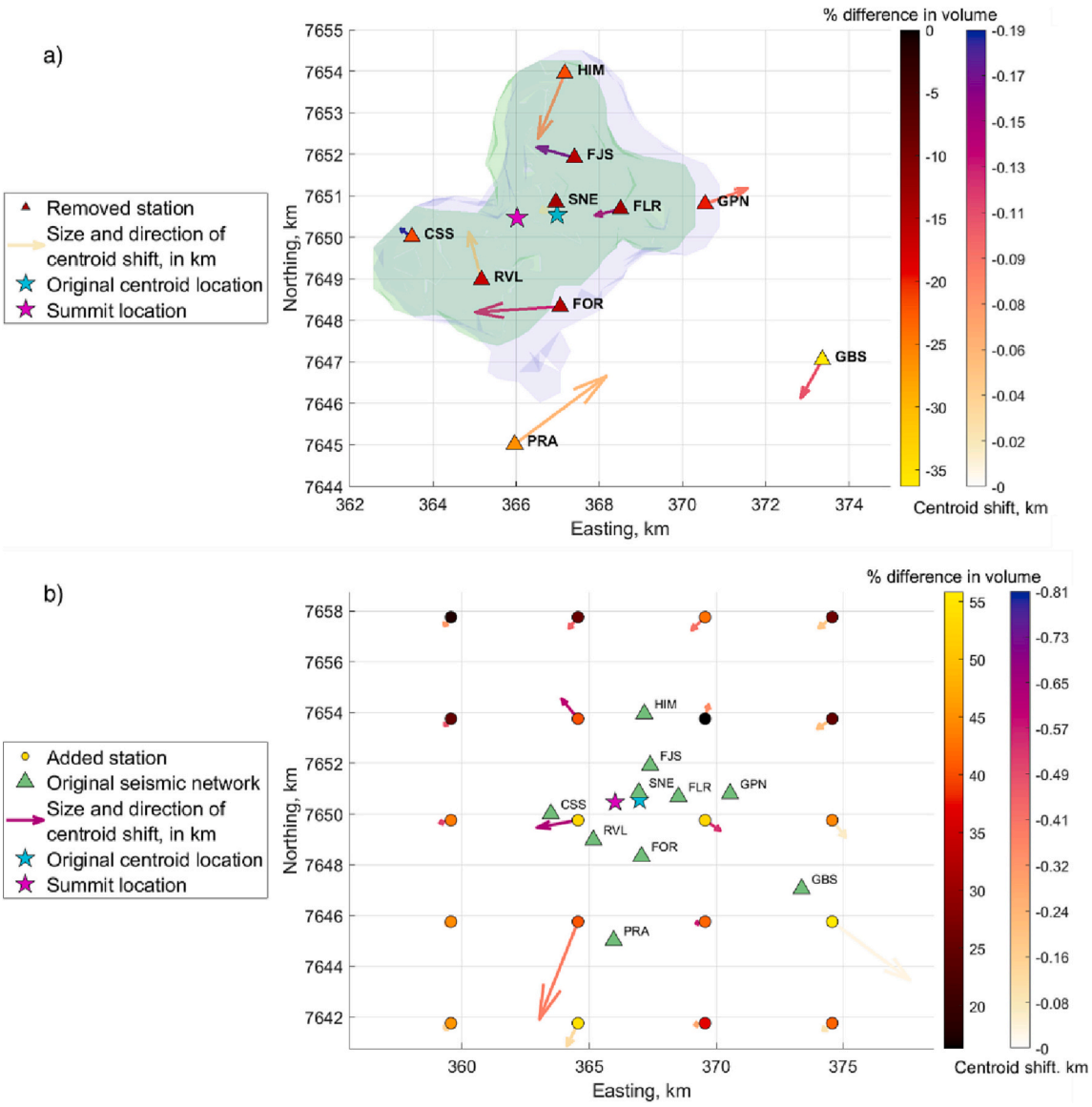

Fig. 12. Reduced (a) and improved (b) simulations for PdF. a) shows the impact that removing a station from the original seismic network has on the DCV size and centroid location. In a), the blue volume shows the original DCV and the green volume shows the DCV when station GBS is removed from the network. For this case the DCV is reduced 37% (see colour of GBS symbol and '% difference in volume' colour bar) and centroid is shifted ~0.1 km south-west. b) shows the impact that adding a new station to the existing seismic network has on the DCV size and centroid location. To make the centroid shifts visible, they have been scaled up by a factor of 3. (For interpretation of the references to colour in this figure legend, the reader is referred to the web version of this article.)

seismic swarm detection methods and apply the analysis to the Global Volcano Monitoring Infrastructure Database GVMID (Costa et al., 2019).

CRediT authorship contribution statement

K.E. James: Conceptualization, Methodology, Software, Writing – original draft, Writing – review & editing, Visualization, Formal analysis. **T. Espinosa-Ortega:** Software, Writing – original draft, Writing – review & editing, Visualization, Formal analysis, Project administration. **C.T. Tan:** Conceptualization, Methodology, Software, Writing – original draft, Writing – review & editing, Visualization, Formal analysis. **B. Taisne:** Supervision, Conceptualization, Methodology, Project administration, Funding acquisition.

Declaration of Competing Interest

The authors declare that they have no known competing financial interests or personal relationships that could have appeared to influence the work reported in this paper.

Data availability

Data will be made available on request.

Acknowledgements

This research was supported by the Earth Observatory of Singapore (EOS) via its funding from the National Research Foundation Singapore and the Singapore Ministry of Education under the Research Centres of Excellence initiative. This work comprises EOS contribution number 479. We also thank the support of the National Research Foundation under ASE. EOS grant numbers 04MNS001816A620OST01, 04MNP001633C210I, NRF2018NRF-NSFC003ES-010.

Code used in this paper is available from: https://github.com/katijam/SARA_CODE

Appendix A. Supplementary data

Supplementary data to this article can be found online at https://doi.org/10.1016/j.jvolgeores.2023.107769.

References

Aki, K., Chouet, B., 1975. Origin of coda waves: source, attenuation, and scattering effects. J. Geophys. Res. 80 (23), 3322–3342. https://doi.org/10.1029/JB080i023p03322.

Aki, K., Richards, P.G., 1980. Quantitative Seismology: Theory and Methods, I. W.H. Freeman, New York, p. 557. https://doi.org/10.1002/gj.3350160110.

Bannister, S., Bryan, C.J., Bibby, H.M., October 2004. (2004) Shear wave velocity variation across the Taupo Volcanic Zone, New Zealand, from receiver function inversion. Geophys. J. Int. 159 (1), 291–310. https://doi.org/10.1111/j.1365-246X.2004.02384.x.

Battaglia, J., Aki, K., 2003. Location of seismic events and eruptive fissures on the Piton de la Fournaise volcano using seismic amplitudes. J. Geophys. Res. 108 (B8), 2364. https://doi.org/10.1029/2002JB002193.

Battaglia, J., Aki, K., Staudacher, T., 2005a. Location of tremor sources and estimation of lava output using tremor source amplitude on the Piton de la Fournaise volcano: 2. Estimation of lava output. J. Volcanol. Geotherm. Res. 147 (3), 291–308. https://doi.org/10.1016/j.jvolgeores.2005.04.006.

Battaglia, J., Aki, K., Ferrazzini, V., 2005b. Location of tremor sources and estimation of lava output using tremor source amplitude on the Piton de la Fournaise volcano: 1. Location of tremor sources. J. Volcanol. Geotherm. Res. 147, 268–290. https://doi.org/10.1016/j.jvolgeores.2005.04.005.

Benoit, J.P., McNutt, S.R., 1996. Global volcanic earthquake swarm database and preliminary analysis of volcanic earthquake swarm duration. Ann. Di Geofis. 39, 221–229.

Caudron, C., Taisne, B., Kugaenko, Y., Saltykov, V., 2015. Magma migration at the onset of the 2012–13 Tolbachik eruption revealed by Seismic Amplitude Ratio Analysis. J. Volcanol. Geotherm. Res. 307, 60–67. https://doi.org/10.1016/j.jvolgeores.2015.09.010.

Caudron, C., White, R.S., Green, R.G., Woods, J., Ágústsdóttir, T., Donaldson, C., Brandsdóttir, B., 2018. Seismic amplitude ratio analysis of the 2014–2015 Bárarbunga-Holuhraun dike propagation and eruption. J. Geophys. Res. Solid Earth 123, 264–276. https://doi.org/10.1002/2017JB014660.

Chávez-García, F., Luzón, F., Raptakis, D., Fernández, J., 2007. Shear-wave velocity structure around Teide Volcano: results using Microtremors with the SPAC Method and Implications for Interpretation of Geodetic results. Pure Appl. Geophys. 164, 697–720. https://doi.org/10.1007/s00024-007-0184-9.

Costa, F., Widiwijayanti, C., Win, N.T.Z., Fajiculay, E., Espinosa-Ortega, T., Newhall, C. G., 2019. WOVOdat – the global volcano unrest database aimed at improving eruption forecasts. Disaster Prev Manag 28 (6), 738–751. https://doi.org/10.1108/DPM-09-2019-0301.

Duputel, Z., Lengliné, O., Ferrazzini, V., 2019. Constraining spatiotemporal characteristics of magma migration at Piton de la Fournaise volcano from pre-eruptive seismicity. Geophys. Res. Lett. 46, 119–127. https://doi.org/10.1029/2018GL080895.

Eibl, E.P., Bean, C.J., Vogfjörd, K.S., Ying, Y., Lokmer, I., Möllhoff, M., Pálsson, F., 2017. Tremor-rich shallow dyke formation followed by silent magma flow at Bárðarbunga in Iceland. Nat. Geosci. 10 (4), 299–304. https://doi.org/10.1038/ngeo2906.

Godfrey, H.J., Fry, B., Savage, M.K., 2017. Shear-wave velocity structure of the Tongariro Volcanic Centre, New Zealand: fast Rayleigh and slow love waves indicate strong shallow anisotropy. J. Volcanol. Geotherm. Res. 336 (33–50) https://doi.org/10.1016/j.jvolgeores.2017.01.019, 0377–0273.

Hofstetter, A., Malone, S.D., 1986. Observations of volcanic tremor at Mount St. Helens in April and May 1980. Bull. Seismol. Soc. Am. 76, 923–938. https://doi.org/10.1785/BSSA0760040923.

Ichihara, M., Matsumoto, S., 2017. Relative Source Locations of Continuous Tremor before and after the Subplinian events at Shinmoe-dake, in 2011. Geophys. Res. Lett. 44 (21), 10,871–10,877. https://doi.org/10.1002/2017GL075293.

Jolly, A., Thompson, G., Norton, G., 2002. Locating pyroclastic flows on Soufriere Hills volcano, Montserrat, West Indies, using amplitude signals from high dynamic range instruments. J. Volcanol. Geotherm. Res. 118, 299–317. https://doi.org/10.1016/S0377-0273(02)00299-8.

Koyanagi, R.Y., Chouet, B., Aki, K., 1987. Origin of volcanic tremor in Hawaii. Part I: Compilation of seismic data from the Hawaiian Volcano Observatory, 1972 to 1985. US Geol. Surv. Prof. Pap. 1350, 1221–1258.

Koyanagi, S., Aki, K., Biswas, N., Mayeda, K., 1995. Inferred attenuation from site effect-corrected T phases recorded on the island of Hawaii, Pure Appl. Geophys. 144, 1–17.

Kumagai, H., Placios, P., Ruiz, M., Yepes, H., Kozono, T., 2011. Ascending seismic source during an explosive eruption at Tungurahua volcano, Ecuador. Geophys. Res. Lett. 38, L01306. https://doi.org/10.1029/2010GL045944.

Kumagai, H., Lacson, R., Maeda, Y., Figueroa, M.S., Yamashina, T., Ruiz, M., Palacios, P., Ortiz, H., Yepes, H., 2013. Source amplitudes of volcano-seismic signals determined by the amplitude source location method as a quantitative measure of event size. J. Volcanol. Geotherm. Res. 257, 57–71. https://doi.org/10.1016/j.jvolgeores.2013.03.002.

Kurokawa, A., Takeo, M., Kurita, K., 2016. Two types of volcanic tremor changed with eruption style during 1986 Izu-Oshima eruption. J. Geophys. Res. Solid Earth 121, 2727–2736. https://doi.org/10.1002/2015JB012500.

Lahr, J.C., Chouet, B.A., Stephens, C.D., Power, J.A., Page, R.A., 1994. Earthquake classification, location, and error analysis in a volcanic environment: Implications for the magmatic system of the 1989–1990 eruptions at Redoubt volcano, Alaska. J. Volcanol. Geotherm. Res. 62, 137–151.

Métaxian, J.P., Santoso, A.B., Caudron, C., Cholik, N., Labonne, C., Poiata, N., Beauducel, F., Monteiller, V., Fahmi, A.A., Rizal, M.H., Nandaka, I.M.A., 2020. Migration of seismic activity associated with phreatic eruption at Merapi volcano, Indonesia. J. Volcanol. Geotherm. Res. 396, 106795 https://doi.org/10.1016/j.jvolgeores.2020.106795.

Morioka, H., Kumagai, H., Maeda, T., 2017. Theoretical basis of the amplitude source location method for volcano-seismic signals. J. Geophys. Res. Solid Earth 122, 6538–6551. https://doi.org/10.1002/2017JB013997.

Observatoire Volcanologique Du Piton De La Fournaise (OVPF), & Institut De Physique Du Globe De Paris (IPGP), 2008. Seismic, Tiltmeter, Extensometer, Magnetic and Weather Permanent Networks on Piton de la Fournaise Volcano and La Réunion. Institut de physique du globe de Paris, Université de Paris. https://doi.org/10.18715/reunion.PF.

Ogiso, M., Yomogida, K., 2012. Migration of tremor locations before the 2008 eruption of Meakandake Volcano, Hokkaido, Japan. J. Volcanol. Geotherm. Res. 217-218, 8–20. https://doi.org/10.1016/j.jvolgeores.2016.06.004.

Passarelli, L., Heryandoko, N., Cesca, S., Rivalta, E., Rasmid, A., Rohadi, S., Dahm, T., Milkereit, C., 2018. Magmatic or not magmatic? The 2015–2016 Seismic Swarm at the Long-Dormant Jailolo Volcano, West Halmahera, Indonesia. Front. Earth Sci. 6, 1–17. https://doi.org/10.3389/feart.2018.00079.

Rubin, A.M., 1993. Tensile fracture of rock at high confining pressure: implications for dike propagation. J. Geophys. Res. 98, 15919. https://doi.org/10.1029/93JB01391.

Rubin, A.M., Gillard, D., 1998. Dike-induced earthquakes: theoretical considerations. J. Geophys. Res. 103, 10,017–10,030. https://doi.org/10.1029/97JB03514.

Taisne, B., Brenguier, F., Shapiro, N.M., Ferrazzini, V., 2011. Imaging the dynamics of magma propagation using radiated seismic intensity. Geophys. Res. Lett. 38, 2–6. https://doi.org/10.1029/2010GL046068.

Takemura, S., Furumura, T., Saito, T., 2009. Distortion of the apparent S-wave radiation pattern in the high-frequency wavefield: Tottori-Ken Seibu, Japan, earthquake of 2000. Geophys. J. Int. 178 (2), 950–961. https://doi.org/10.1111/J.1365-246X.2009.04210.X.

Tan, C.T., Taisne, B., Neuberg, J., Basuki, A., 2019. Real-time assessment of potential seismic migration within a monitoring network using Red-flag SARA. J. Volcanol. Geotherm. Res. 384, 31–47. https://doi.org/10.1016/j.jvolgeores.2019.07.004.

Tanaka, S., Hamaguchi, H., Ueki, S., Sato, M., Nakamichi, H., 2002. Migration of seismic activity during the 1998 volcanic unrest at Iwate Volcano, Northeastern Japan, with reference to P and S wave velocity anomaly and crustal deformation. J. Volcanol. Geotherm. Res. 113, 399–414. https://doi.org/10.1016/S0377-0273(01)00273-6.

Walsh, B., Jolly, A.D., Procter, J., 2017. Calibrating the amplitude source location (ASL) method by using active seismic sources: an example from Te Maari volcano, Tongariro National Park, New Zealand. Geophys. Res. Lett. 44 (8), 3591–3599. https://doi.org/10.1002/2017G L073000.

Yamasato, H., 1997. Quantitative analysis of pyroclastic flows using infrasonic and seismic data at Unzen volcano, Japan. J. Phys. Earth 45 (6), 397–416.

Zobin, V.M., Sudo, Y., 2017. Source properties of Strombolian explosions at Aso volcano, Japan, derived from seismic signals. Phys. Earth Planet. Inter. 268, 1–10. https://doi.org/10.1016/j.pepi.2017.05.002.